# A1 Resonators in 128° Y-cut Lithium Niobate with Electromechanical Coupling of 46.4%

Ruochen Lu, *Member, IEEE*, Yansong Yang, *Member, IEEE*, Steffen Link, *Student Member, IEEE*, and Songbin Gong, *Senior Member, IEEE*

***Abstract*— In this work, we present first-order antisymmetric (A1) mode resonators in 128° Y-cut lithium niobate ($LiNbO_3$) thin films with electromechanical coupling coefficients ($k^2$) as large as 46.4%, exceeding the state-of-the-art. The achievable $k^2$ of A1 in $LiNbO_3$ substrates of different orientations is first explored, showing X-axis direction in 128° Y-cut $LiNbO_3$ among the optimal combinations. Subsequently, A1 resonators with spurious mode mitigation are designed and fabricated. In addition to the large $k^2$, the implemented devices show a maximum quality factor ($Q$) of 598 at 3.2 GHz. Upon further optimization, the reported platform can potentially deliver a wideband acoustic-only filtering solution in 5G New Radio. [2020-0003]**

***Index Terms*— 5G new radio, acoustic resonators, Lamb wave, lithium niobate, microelectromechanical devices, piezoelectric devices.**

## I. Introduction

THE emerging fifth-generation (5G) wireless communication is calling for unprecedented signal processing in different application scenarios [1], [2]. More specifically, the enhanced mobile broadband (eMBB), where a 1000-fold increase in mobile data volume is envisioned [3], requires wide bandwidth at higher center frequencies. Recently, the Third Generation Partnership Project (3GPP) has released the first set of specifications for 5G bands [4]. Radio frequency (RF) spectrum at 3-6 GHz is of great value for 5G deployment as it offers front-end designers well-balanced trades between large available bandwidth and low free path loss. As long as the essential components, e.g., acoustic filters, can be designed to accommodate the specifications of the 5G New Radio (NR) bands [4], sub-6GHz 5G systems can see rapid expansion in use scenarios.

However, transitioning from 4G LTE acoustic filters to 5G NR is not trivial. The foremost challenge is the insufficient fractional bandwidth (FBW) of the current acoustic filters based on the surface acoustic wave (SAW) [5], [6], or film bulk acoustic resonator (FBAR) [7], [8]. Different from LTE bands ranging from 0.4 to 3.6 GHz with a maximum FBW around 4%, the proposed 5G NR bands entail FBW as large as 24% (n77 band, 3.3 GHz to 4.2 GHz) [4], which requires an effective electromechanical coupling coefficient ($k^2$) [9] no less than 50% if the ladder-type filters are used [10]. To enhance FBW of the acoustic filters, different approaches have been investigated, including transferred thin films on costly substrates [11]–[14], new materials with larger piezoelectric coefficients [15]–[20], and incorporating additional lumped elements or transmission lines [21]–[23]. However, none of the reported solutions are so far adequate for achieving 24% FBW.

Among these solutions, the first-order antisymmetric (A1) Lamb mode devices in Z-cut lithium niobate ($LiNbO_3$) is the closest. A1 resonators have been demonstrated with $k^2$ as large as 30% and low damping around the sub-6 GHz NR bands with large feature sizes [24]–[28], thanks to the large $e_{15}$ of 3.76 C/m$^2$ in Z-cut $LiNbO_3$ [29]. FBW up to 12.5% has been achieved by ladder filters constructed with A1 resonators [30], [31]. However, it is still far from the required 24% FBW of n77, therefore calling for an acoustic platform with even larger $k^2$.

In this work, we report A1 resonators in 128° Y-cut $LiNbO_3$ thin films with $k^2$ as large as 46.4%, significantly exceeding the state-of-the-art. A1 resonators with spurious mode mitigation have been designed and fabricated. In addition to the large $k^2$, the implemented devices show a maximum quality factor ($Q$) of 598 at 3.2 GHz. Upon further optimization, the reported platform can potentially deliver a wideband acoustic-only filtering solution for 5G NR. The paper is organized as follows. Section II first explores the orientations for achieving high $k^2$ for A1, followed by introducing the design of A1 resonators with spurious mode mitigation. Section III presents the fabricated A1 resonators. Section IV shows the measured results and extracted high $k^2$. Finally, the conclusion is stated in Section V.

## II. A1 Mode Resonator Design

### A. $LiNbO_3$ Orientation Selection

Rotated Y-cut $LiNbO_3$ substrates are studied in this work due to their commercial availability. In a rotated Y-cut $LiNbO_3$ with rotation $\Psi$, the X-axis of the material is within the substrate and the normal vector (**n**) of the substrate is rotated $\Psi$ from the Y-axis about the material X-axis. We further define that the A1 wave propagates along the vector (**l**), which is $\varphi$

Manuscript received January 3, 2020; revised March 17, 2020; accepted March 19, 2020. Date of publication April 2, 2020; date of current version June 2, 2020. Subject Editor E. Kim. *(Corresponding author: Ruochen Lu.)*

The authors are with the Department of Electrical and Computing Engineering, University of Illinois at Urbana–Champaign, Urbana, IL 61801 USA (e-mail: rlu10@illinois.edu).

Color versions of one or more of the figures in this article are available online at http://ieeexplore.ieee.org.

Digital Object Identifier 10.1109/JMEMS.2020.2982775

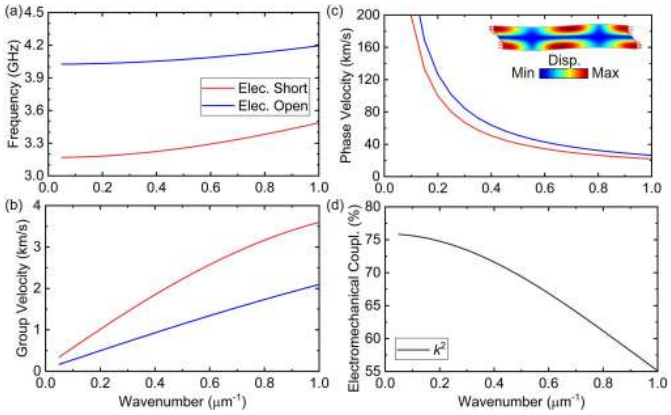


Fig. 1. FEA simulated A1 characteristics with different wavenumbers in a 550 nm thick 128° Y $LiNbO_3$ thin film. (a) Frequency, (b) phase velocity, and (c) group velocity with electrically open and short boundary conditions. (d) $k^2$ versus wavenumber. Displacement mode shape of A1 is presented.

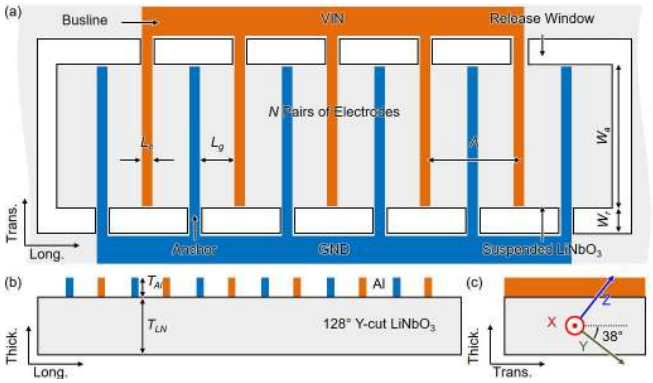


Fig. 2. Mockup of an A1 resonator in a suspended 128° Y-cut $LiNbO_3$ thin film. (a) Top view, (b) front view, and (c) side view.

TABLE I
DESIGN PARAMETERS OF THE A1 RESONATOR

| Sym. | Parameter | Value | Sym. | Parameter | Value |
|---|---|---|---|---|---|
| $\Lambda$ | Cell length (μm) | 20-40 | $W_a$ | Aperture width (μm) | 65 |
| $L_e$ | Electrode length (μm) | 3-4 | $W_r$ | Release window width (μm) | 8 |
| $L_g$ | Gap length (μm) | 6-17 | $T_{LN}$ | $LiNbO_3$ thickness (nm) | 550 |
| $N$ | No. of electrode pairs | 5-10 | $T_{Al}$ | Aluminum thickness (nm) | 300 |

from the material X-axis when rotated around **n**. Therefore, A1 propagates along the cross-section that includes **n** and **l**. The material constants in the cross-section can be obtained by transforming the original matrices [29] using the Euler angles ($\lambda$, $\mu$, $\theta$) [32]. The Euler angle is defined as the rotation from the material axis to the device axis, following the Z−X−Z convention [32]. For a rotated Y-cut $LiNbO_3$ with rotation $\Psi$, the Euler angles are $\lambda = \theta = 0$ and $\mu = \Psi - 90°$ [32]. More specifically, the Euler angle for the cross-section along the X-axis in 128° Y-cut $LiNbO_3$ is (0°, 38°, 0°) [32]. Details can be found in Section 4-4 of [32]. 128° Y-cut $LiNbO_3$ features a significant piezoelectric constant $e_{15}$ of 4.47 $C/m^2$ [33], promising a large $k^2$, as suggested by prior works [28]. Moreover, 128° Y-cut $LiNbO_3$ features zero piezoelectric constants $e_{11}$, $e_{12}$, $e_{13}$, $e_{14}$, and a significantly smaller coefficient $e_{16}$ for the shear horizontal mode (0.28 $C/m^2$) compared to $e_{15}$ of A1 mode (4.47 $C/m^2$). Such results indicate that laterally excited A1 resonators 128° Y-cut $LiNbO_3$ are less prone to have the shear horizontal and symmetrical spurious overtones when compared to Z-cut $LiNbO_3$ [27].

To more accurately capture the A1 characteristics, 550 nm thick 128° Y-cut $LiNbO_3$ is studied using finite element analysis (FEA). The two-dimensional (2D) eigenmode simulation is set up following the same procedure in [34]. The simulated frequencies of A1 under electrically short on the top surface ($f_{short}$) and open conditions ($f_{open}$) with different wavenumbers ($\beta$) are plotted in Fig. 1 (a). Similar to the Z-cut case [27], cut off frequencies are observed, 4.02 GHz for $f_{open}$, and 3.17 GHz for $f_{short}$. The frequency increases for a larger $\beta$, showing the frequency tuning of A1. Moreover, based on the eigenmode analysis, the phase velocity $v_p$, group velocity $v_g$, and $k^2$ can be calculated by [35]–[37]:

$$v_{p\_short} = 2\pi f_{short}/\beta, v_{p\_open} = 2\pi f_{open}/\beta, \quad (1)$$

$$v_{g\_short} = 2\pi \partial f_{short}/\partial\beta, v_{g\_open} = 2\pi \partial f_{open}/\partial\beta \quad (2)$$

$$k^2 = \pi^2/8 \cdot [(v_{p\_open}/v_{p\_short})^2 - 1] \quad (3)$$

The obtained values are plotted in Fig. 1 (b) – (d), respectively. A maximum $k^2$ of 75.8% is obtained near the cut-off. High phase velocities beyond 40000 m/s, low group velocities below 2500 m/s, and more importantly, $k^2$ beyond 70% are obtained for $\beta$ less than 0.5 $\mu m^{-1}$ (or wavelength longer than 12.6 $\mu$m), marking the feasibility of wideband operation in 5G NR bands using A1 mode resonators in 128° Y-cut $LiNbO_3$ with large feature sizes.

### B. Resonator Design Overview

The mockup view of a typical A1 resonator is shown in Fig. 2 with the key parameters explained in Table I. The resonator is composed of 300 nm thick aluminum (Al) interdigitated electrodes (IDTs) on the top of a suspended 550 nm thick 128° Y-cut $LiNbO_3$ thin film. As presented in Section II-A, the longitudinal direction is along the X-axis of $LiNbO_3$ for maximizing the $k^2$, and the thickness of $LiNbO_3$ is selected for enabling an operating frequency around 3.3 GHz for 5G NR bands. The material axes are labeled in Fig. 2 (c). $N$ pairs of IDTs, with a cell length of $\Lambda$, are alternatingly connected to the signal and ground. The electrode length ($L_e$) and gap length ($L_g$) are labeled. A pair of additional $LiNbO_3$ slabs with a width of $\Lambda/2$ are included at the longitudinal ends to maintain the periodicity in the structure. $\Lambda$, $L_e$, and $N$ are selected based on the spurious mode suppression approach described in [26], [38]. More specifically, $L_e$ is set to be much less than $L_g$ to mitigate the spurious modes, while maintaining a high $Q$ for the main mode. However, such an approach is at the cost of reduced $k^2$ because of the fringe electrical field outside the $LiNbO_3$ thin film, which does not contribute to the piezoelectric transduction and acts as a feedthrough capacitance between IDTs. The effects will be quantitatively studied in Section II-C. The buslines are placed outside the active region to avoid additional spurious modes and also to minimize the feedthrough capacitance between the buslines.

TABLE II
EXTRACTED KEY PARAMETERS FROM DEVICE A SIMULATION

| Sym. | Value | Sym. | Value | Sym. | Value |
|---|---|---|---|---|---|
| $C_0$ | 12.40 fF | $L_s$ | 0 nH | $n$ | 10 |
| $f_{s1}$ | 3.21 GHz | $k_1^2$ | 49.7% | $Q_1$ | 499 |
| $f_{s2}$ | 3.24 GHz | $k_2^2$ | 4.60% | $Q_2$ | 539 |
| $f_{s3}$ | 2.54 GHz | $k_3^2$ | 0.74% | $Q_3$ | 548 |
| $f_{s4}$ | 2.63 GHz | $k_4^2$ | 0.45% | $Q_4$ | 450 |
| $f_{s5}$ | 2.75 GHz | $k_5^2$ | 0.18% | $Q_5$ | 458 |
| $f_{s6}$ | 3.70 GHz | $k_6^2$ | 0.08% | $Q_6$ | 469 |
| $f_{s7}$ | 3.89 GHz | $k_7^2$ | 0.05% | $Q_7$ | 529 |
| $f_{s8}$ | 9.55 GHz | $k_8^2$ | 6.64% | $Q_8$ | 480 |
| $f_{s9}$ | 16.1 GHz | $k_9^2$ | 2.09% | $Q_9$ | 490 |
| $f_{s10}$ | 22.9 GHz | $k_{10}^2$ | 1.11% | $Q_{10}$ | 478 |

TABLE III
DESIGN PARAMETERS OF THE IMPLEMENTED A1 RESONATORS

| Design | $\Lambda$ (μm) | $L_e$ (μm) | $L_g$ (μm) | $N$ (μm) | $W_a$ (μm) |
|---|---|---|---|---|---|
| Device A | 40 | 3 | 17 | 5 | 65 |
| Device B | 30 | 4 | 11 | 5 | 65 |
| Device C | 20 | 4 | 6 | 10 | 65 |

### *C. Device Simulation and Key Parameter Extraction*

To capture the design intricacies, 2D frequency-domain FEA is performed, with the dimensions of Device A in Table III ($\Lambda$ of 40 $\mu$m, $L_e$ of 3 $\mu$m, and $N$ of 5). A mechanical $Q$ of 500 is adopted by setting a complex stiffness constant. This $Q$ value is empirical, based on previous experimental results in similar film stacks [25], [26]. The other loss mechanisms are not included due to the inadequate study on loss in A1 resonators so far. Note that the simplified 2D FEA does not include the effects in the transverse direction.

The wideband admittance response (0.01 – 24 GHz) is presented in Fig. 3 (a). Only the odd-order antisymmetric modes are efficiently excited, validating our earlier findings in Section II-A on the clean spectrum in 128° Y-cut $LiNbO_3$. The zoomed-in admittance of A1 is shown in Fig. 3 (b) and (c) in amplitude and phase, respectively. The A1 resonance is observed at 3.21 GHz, agreeing with that calculated in Fig. 1 (a). A perceived $k^2$ of 50.2% is obtained, calculated from the frequency with the maximum admittance $f_s$ and the frequency with the minimum admittance $f_p$ using [9], [35], [37]:

$$k^2_{perceived} = \pi^2/8 \cdot [(f_p/f_s)^2 - 1] \tag{4}$$

Such a value is smaller than that simulated from the eigenmode FEA [Fig.1 (d)]. Such $k^2$ reduction is due to the fringe electrical field introduced by the spurious mode suppression design in Section II-B. The simulation includes an air box surrounding the resonator to capture the fringe electrical feedthrough from the air above and below the resonant body. This airbox was not included in the eigenmode analysis. In this case, the fringe field contributes to 4.12 fF, in addition to the capacitance of 8.28 fF from the lateral field in the $LiNbO_3$ thin film. Therefore, the perceived $k^2$ reduced from 73.9% to the obtained value of 50.2%. Such an effect can be mitigated by scaling down $L_e$ and $\Lambda$ simultaneously [38]. Upon further optimization, a spurious-free A1 resonator with $k^2$ beyond 65% is feasible. Nevertheless, the simulated $k^2$ in the prototype is still significantly larger than those in the prior reports. The vibrational mode shapes of A1 are plotted in Fig. 3 (d) for both the displacement amplitude and stress ($T_{xz}$) fields.

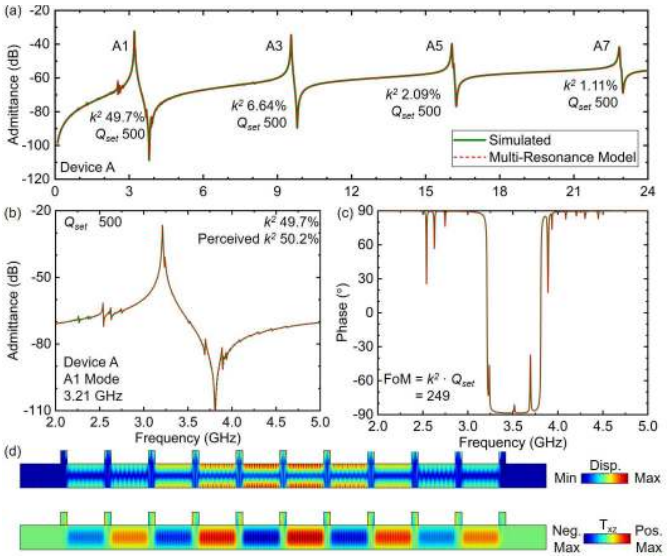


Fig. 3. FEA simulated results of Device A. (a) Wideband admittance response. Zoomed-in A1 mode admittance response in (b) amplitude and (c) phase. (d) Simulated displacement amplitude and stress mode shape at the A1 resonance.

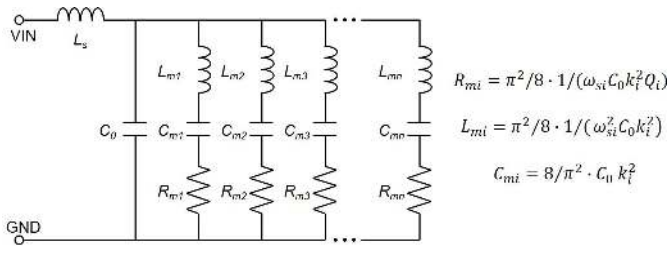


Fig. 4. Multi-resonance MBVD model for extracting key parameters.

To more accurately extract $k^2$ from the simulation, the multi-resonance MBVD model is used (Fig. 4). The model includes different motional branches, which have been shown crucial for extracting parameters of resonators with significant $k^2$ [37]. A series inductor $L_s$ is included for the high-frequency response. The extracted parameters are listed in Table II. The admittance of the model using the extracted parameters is plotted in Fig. 3, showing excellent agreement. The static capacitance ($C_0$) is 12.4 fF. The A1 mode at 3.21 GHz has a $k^2$ of 49.7%, which is slightly less than the perceived $k^2$ of 50.2%, because of the spurious mode at 3.24 GHz with a $k^2$ of 4.60% (mode 2 in Table II). The other in-band spurious modes (between $f_s$ and $f_p$) are successfully mitigated, showing $k^2$ less than 0.1% (modes 6 – 7 in Table II). The extracted $Q$ is 499. The discrepancy between the set value (500) and the extracted value is caused by the finite number

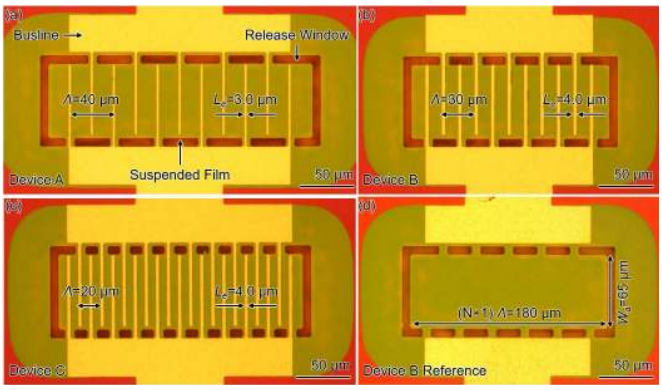


Fig. 5. Optical images of the implemented A1 resonators with the key parameters labeled. (a) Device A, (b) Device B, (c) Device C, and (d) reference structure for Device B.

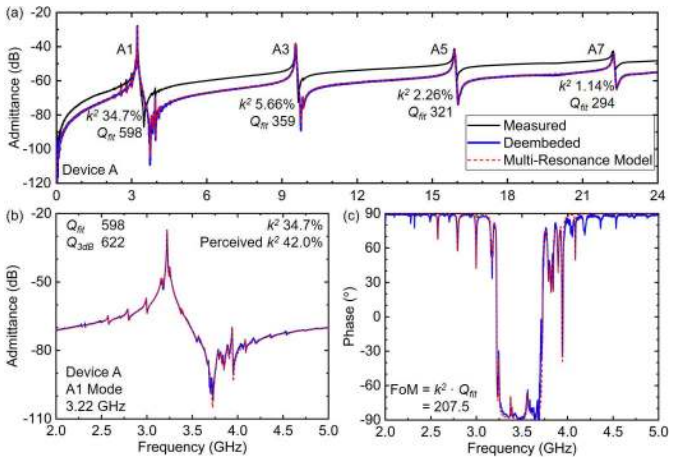


Fig. 6. Measured performance of Device A. (a) Wideband admittance response. Zoomed-in A1 mode admittance response in (b) amplitude and (c) phase.

of points in the simulation. The simulation validates A1 in 128° Y-cut $LiNbO_3$ thin film as a promising wideband acoustic filtering solution for 5G NR.

The parameters of the higher-order antisymmetric modes are also extracted (modes 8 – 10 in Table II). The A3 mode at 9.55 GHz has a $k^2$ of 6.64%, while the A5 mode at 16.1 GHz has a $k^2$ of 2.09%. The A7 mode at 22.9 GHz has a $k^2$ of 1.11%, suggesting potential applications also at higher frequencies using the proposed platform [39].

## III. Device Fabrication

The devices were fabricated following the process in [40]. A 550 nm 128° Y-cut $LiNbO_3$ thin film on a 4-inch Si wafer is provided by NGK Insulators, Ltd., for the fabrication. After defining the release windows using inductively coupled plasma reactive ion etching, the top 300 nm Al electrodes were evaporated. The devices were finally released by $XeF_2$ etching. The resistivity of the high-resistivity silicon substrate is above 4000 Ω·cm. The finite resistivity causes additional undesired feedthrough, especially near the high impedance regime near the anti-resonance [41].

The optical images of the implemented devices are shown in Fig. 5, with the design parameters listed in Table III. For each design, a reference device that has an identical layout to the design except for the absence of IDTs, is implemented [Fig. 5 (d)]. The reference devices are used to evaluate the effects of the feedthrough path introduced by the probing pads.

## IV. Measurement and Discussion

The implemented resonators were first measured with an Agilent N5230A network analyzer at the −10 dBm power level in the air. Device A [Fig. 5 (a), $\Lambda$ of 40 $\mu$m, $L_e$ of 3 $\mu$m, and $N$ of 5] is first analyzed. The admittance is plotted in Fig. 6. The deembeded performance is obtained by subtracting the admittance of the reference device from the measured admittance. In doing so, the feedthrough from the pads and buslines are removed, suggesting the maximum $k^2$ and impedance ratio that one may achieve through design optimizations. As seen in Fig. 6 (a), the wideband performance shows that only the odd-order antisymmetric modes

TABLE IV
Extracted Key Parameters from Device A Measurement

| Sym. | Value | Sym. | Value | Sym. | Value |
|---|---|---|---|---|---|
| $C_0$ | 12.60 fF | $L_s$ | 0.10 nH | $n$ | 17 |
| $f_{s1}$ | 3.22 GHz | $k_1^2$ | 34.7% | $Q_1$ | 598 |
| $f_{s2}$ | 3.25 GHz | $k_2^2$ | 6.09% | $Q_2$ | 327 |
| $f_{s3}$ | 3.16 GHz | $k_3^2$ | 1.12% | $Q_3$ | 520 |
| $f_{s4}$ | 3.17 GHz | $k_4^2$ | 3.75% | $Q_4$ | 268 |
| $f_{s5}$ | 3.18 GHz | $k_5^2$ | 0.70% | $Q_5$ | 505 |
| $f_{s6}$ | 2.58 GHz | $k_6^2$ | 0.35% | $Q_6$ | 307 |
| $f_{s7}$ | 2.79 GHz | $k_7^2$ | 1.01% | $Q_7$ | 196 |
| $f_{s8}$ | 3.00 GHz | $k_8^2$ | 1.14% | $Q_8$ | 375 |
| $f_{s9}$ | 3.38 GHz | $k_9^2$ | 0.16% | $Q_9$ | 670 |
| $f_{s10}$ | 3.56 GHz | $k_{10}^2$ | 0.26% | $Q_{10}$ | 109 |
| $f_{s11}$ | 3.79 GHz | $k_{11}^2$ | 0.10% | $Q_{11}$ | 237 |
| $f_{s12}$ | 3.82 GHz | $k_{12}^2$ | 0.19% | $Q_{12}$ | 140 |
| $f_{s13}$ | 3.89 GHz | $k_{13}^2$ | 0.14% | $Q_{13}$ | 204 |
| $f_{s14}$ | 3.94 GHz | $k_{14}^2$ | 0.19% | $Q_{14}$ | 625 |
| $f_{s15}$ | 9.55 GHz | $k_{15}^2$ | 5.66% | $Q_{15}$ | 359 |
| $f_{s16}$ | 15.9 GHz | $k_{16}^2$ | 2.26% | $Q_{16}$ | 321 |
| $f_{s17}$ | 22.2 GHz | $k_{17}^2$ | 1.14% | $Q_{17}$ | 294 |

are efficiently excited with lateral electrical fields in 128° Y-cut $LiNbO_3$. The A1 resonance shows a perceived $k^2$ of 42.0% (Eq. 4) and a 3-dB $Q$ of 622 [Fig. 6 (b) (c)]. The reason for a higher $Q$ than the prior A1 resonators in Z-cut $LiNbO_3$ requires further investigation. More spurious modes are observed compared to the simulated results in Fig. 4, likely caused by the effects in the transverse direction that are not captured in 2D FEA. The multi-resonance MBVD model is used to accurately extract the key parameters (Table IV). A1 has a $k^2$ of 34.7%, and a $Q$ of 598. The discrepancy between the extracted $k^2$ and the perceived $k^2$ is caused by a series of high coupling modes next to the main mode (modes

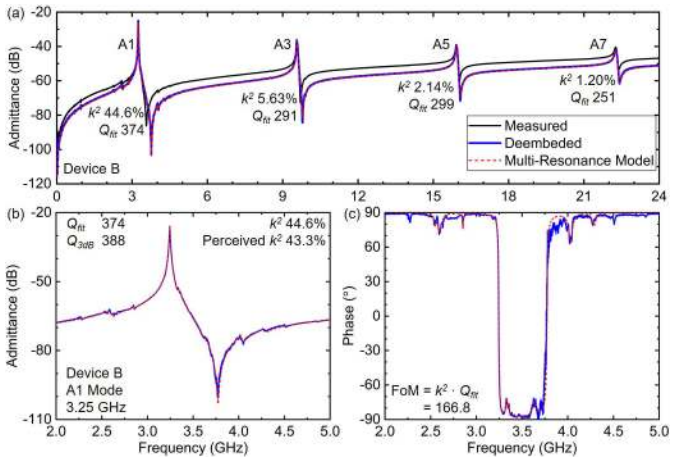


Fig. 7. Measured performance of Device B. (a) Wideband admittance response. Zoomed-in A1 mode admittance response in (b) amplitude and (c) phase.

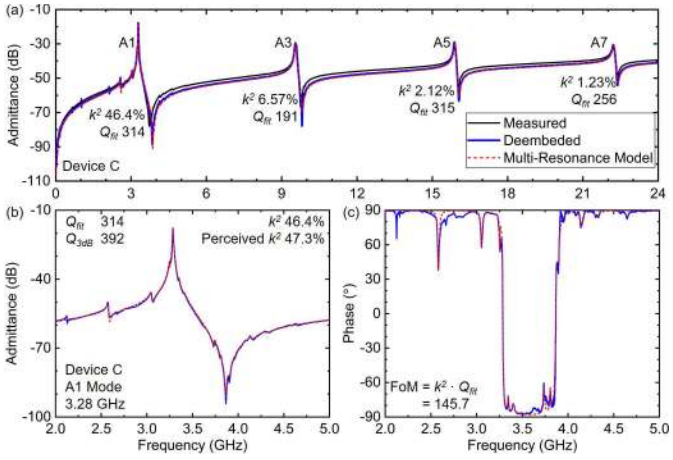


Fig. 8. Measured performance of Device C. (a) Wideband admittance response. Zoomed-in A1 mode admittance response in (b) amplitude and (c) phase.

TABLE V
EXTRACTED KEY PARAMETERS FROM DEVICE B MEASUREMENT

| Sym. | Value | Sym. | Value | Sym. | Value |
|---|---|---|---|---|---|
| $C_0$ | 18.28 fF | $L_s$ | 0.20 nH | $n$ | 12 |
| $f_{s1}$ | 3.25 GHz | $k_1^2$ | 44.6% | $Q_1$ | 374 |
| $f_{s2}$ | 3.33 GHz | $k_2^2$ | 1.14% | $Q_2$ | 161 |
| $f_{s3}$ | 2.54 GHz | $k_3^2$ | 0.43% | $Q_3$ | 99 |
| $f_{s4}$ | 2.60 GHz | $k_4^2$ | 1.40% | $Q_4$ | 55 |
| $f_{s5}$ | 2.85 GHz | $k_5^2$ | 0.25% | $Q_5$ | 302 |
| $f_{s6}$ | 3.36 GHz | $k_6^2$ | 0.23% | $Q_6$ | 390 |
| $f_{s7}$ | 3.63 GHz | $k_7^2$ | 0.19% | $Q_7$ | 62 |
| $f_{s8}$ | 4.03 GHz | $k_8^2$ | 0.24% | $Q_8$ | 83 |
| $f_{s9}$ | 4.29 GHz | $k_9^2$ | 0.14% | $Q_9$ | 93 |
| $f_{s10}$ | 9.57 GHz | $k_{10}^2$ | 5.64% | $Q_{10}$ | 291 |
| $f_{s11}$ | 15.9 GHz | $k_{11}^2$ | 2.14% | $Q_{11}$ | 299 |
| $f_{s12}$ | 22.3 GHz | $k_{12}^2$ | 1.20% | $Q_{12}$ | 251 |

TABLE VI
EXTRACTED KEY PARAMETERS FROM DEVICE C MEASUREMENT

| Sym. | Value | Sym. | Value | Sym. | Value |
|---|---|---|---|---|---|
| $C_0$ | 52.79 fF | $L_s$ | 0.15 nH | $n$ | 12 |
| $f_{s1}$ | 3.29 GHz | $k_1^2$ | 46.4% | $Q_1$ | 314 |
| $f_{s2}$ | 3.24 GHz | $k_2^2$ | 2.04% | $Q_2$ | 482 |
| $f_{s3}$ | 3.34 GHz | $k_3^2$ | 0.89% | $Q_3$ | 279 |
| $f_{s4}$ | 2.58 GHz | $k_4^2$ | 1.91% | $Q_4$ | 135 |
| $f_{s5}$ | 3.05 GHz | $k_5^2$ | 1.81% | $Q_5$ | 144 |
| $f_{s6}$ | 3.40 GHz | $k_6^2$ | 0.67% | $Q_6$ | 116 |
| $f_{s7}$ | 3.74 GHz | $k_7^2$ | 0.08% | $Q_7$ | 211 |
| $f_{s8}$ | 3.89 GHz | $k_8^2$ | 0.04% | $Q_8$ | 117 |
| $f_{s9}$ | 4.14 GHz | $k_9^2$ | 0.08% | $Q_9$ | 133 |
| $f_{s10}$ | 9.56 GHz | $k_{10}^2$ | 6.57% | $Q_{10}$ | 191 |
| $f_{s11}$ | 15.9 GHz | $k_{11}^2$ | 2.12% | $Q_{11}$ | 256 |
| $f_{s12}$ | 22.2 GHz | $k_{12}^2$ | 1.23% | $Q_{12}$ | 251 |

2 – 5 in Table IV). Such a $k^2$ is larger than the previously reported values in A1 resonators in $LiNbO_3$. The other in-band spurious modes are mitigated, showing $k^2$ less than 0.2% (modes 9 – 14 in Table IV). Further spurious mode suppression is required for alternative $Q$ representations, such as Bode $Q$ across the spectrum or 3-dB $Q$ at the anti-resonance [42], which can be essential for filter applications. Higher-order antisymmetric modes are also observed (modes 15 – 17 in Table IV), including A3 at 9.55 GHz with a $k^2$ of 5.66% and a $Q$ of 359, A5 at 15.9 GHz with a $k^2$ of 2.26% and a $Q$ of 321, and A7 at 22.2 GHz with a $k^2$ of 1.14% and a $Q$ of 294.

Device B [Fig. 5 (b), $\Lambda$ of 20 $\mu$m, $L_e$ of 4 $\mu$m, and $N$ of 5] is then analyzed. A1 shows a perceived $k^2$ of 43.3% (Eq. 4) and a 3-dB $Q$ of 388 (Fig. 7). The spectrum near A1 is cleaner than Device A. However, $Q$ is reduced because of a larger metal coverage ratio that leads to a higher loss from acoustic damping in Al [40]. The extracted parameters of different modes are listed in Table V. A1 has a $k^2$ of 44.6%, and a $Q$ of 374, close to the perceived $k^2$ due to the few spurious modes near the main mode. $k^2$ of Device B is larger than that in Device A, because of the less fringe electrical field. The in-band spurious modes (modes 6 – 7 in Table V) are mitigated, showing $k^2$ around 0.2%. Higher-order antisymmetric modes (modes 10 – 12 in Table V) are A3 at 9.57 GHz with a $k^2$ of 5.64%, and a $Q$ of 291, A5 at 15.9 GHz with a $k^2$ of 2.14%, and a $Q$ of 299, and A7 at 22.3 GHz with a $k^2$ of 1.20%, and a $Q$ of 251.

Next, Device C [Fig. 5 (c), $\Lambda$ of 10 $\mu$m, $L_e$ of 4 $\mu$m, and $N$ of 10] is analyzed. The device has an even smaller $\Lambda$ than device B. It is expected to yield slightly larger $k^2$ due to the proportionally less significant fringe field, but a worse $Q$ from a larger metal coverage ratio. A1 shows a perceived $k^2$ of 47.3% (Eq. 4) and a 3-dB $Q$ of 392 (Fig. 8). The extracted parameters of different modes are listed in Table VI. A1 has a $k^2$ of 46.4%, and a $Q$ of 314. The large $k^2$ significantly

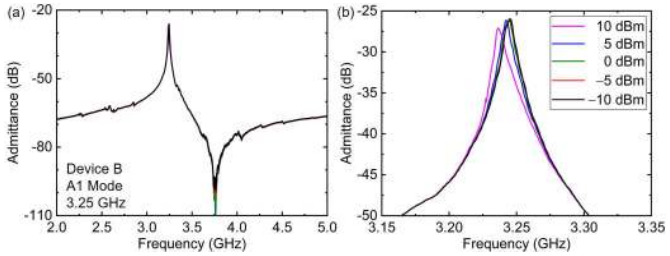


Fig. 9. Measured (a) wideband, and (b) zoomed-in nonlinear admittance response of Device B at different power levels.

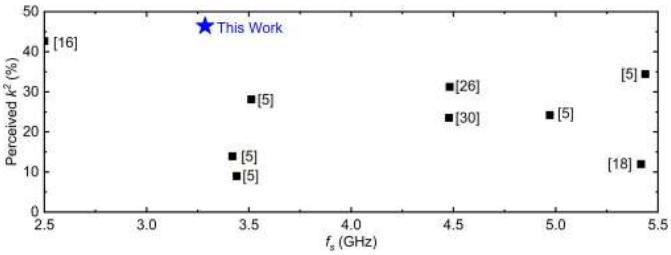


Fig. 10. Comparison of the reported A1 resonator in 128° Y-cut $LiNbO_3$ with prior reports, in terms of $k^2$ and operating frequency. $k^2$ of different reports are all calculated using Eq. 4 for fair comparison.

surpasses those of previous A1 resonators, confirming our analysis in Section II-A. The in-band spurious modes (modes 6 – 8 in Table VI) are mitigated. Higher-order antisymmetric modes (modes 10 – 12 in Table VI) are A3 at 9.56 GHz with a $k^2$ of 6.57%, and a $Q$ of 191, A5 at 15.9 GHz with a $k^2$ of 2.12%, and a $Q$ of 256, and A7 at 22.2 GHz with a $k^2$ of 1.23%, and a $Q$ of 251. The large $k^2$ of A3 is also among the highest in acoustic resonators around 10 GHz.

The nonlinearity of the device is investigated (Fig. 9). Device B is measured at different power levels from −10 dBm to 10 dBm in air. The device performance is mostly linear [Fig. 9 (a)] except for the part near the resonance [Fig. 9 (b)]. The thermally induced nonlinearity [43] can be observed at 10 dBm. Thermal handling capabilities can be further enhanced through techniques such as fully anchored designs.

Finally, the performance is compared to the state-of-the-art (Fig. 10). $k^2$ and operating frequencies of the prior works in the frequency range between 2.5 GHz to 5.5 GHz are plotted [5], [16], [18], [26], [30]. Because $k^2$ are calculated differently in different papers, Eq. 4 is used here to calculate the perceived $k^2$ using the reported $f_s$ and $f_p$. The $k^2$ obtained in this work has surpassed the state-of-the-art. It is noteworthy that the A1 resonator prototypes are still far from the full potential of the 128° Y-cut $LiNbO_3$ platform. Based on optimized designs (e.g., simultaneously narrowed $L_e$ and $\Lambda$ [38]), wideband A1 resonators with $k^2$ of 65% and spurious mode mitigated can be expected.

## V. Conclusion

In this work, A1 resonators in 128° Y-cut $LiNbO_3$ thin films with $k^2$ as large as 46.4% have been demonstrated, significantly surpassing the state-of-the-art. In addition to the large $k^2$, the implemented A1 resonators show a maximum $Q$ of 598 at 3.2 GHz with spurious modes mitigated. Upon further optimization, the reported platform can potentially deliver a wideband acoustic-only filtering solution for 5G NR.

## References

[1] S. Parkvall, E. Dahlman, A. Furuskar, and M. Frenne, "NR: The new 5G radio access technology," *IEEE Commun. Standards Mag.*, vol. 1, no. 4, pp. 24–30, Dec. 2017.

[2] P. Popovski, K. F. Trillingsgaard, O. Simeone, and G. Durisi, "5G wireless network slicing for eMBB, URLLC, and mMTC: A communication-theoretic view," *IEEE Access*, vol. 6, pp. 55765–55779, 2018.

[3] A. Anand, G. De Veciana, and S. Shakkottai, "Joint scheduling of URLLC and eMBB traffic in 5G wireless networks," in *Proc. IEEE INFOCOM Conf. Comput. Commun.*, Feb. 2018, pp. 1970–1978.

[4] J. Lee *et al.*, "Spectrum for 5G: Global status, challenges, and enabling technologies," *IEEE Commun. Mag.*, vol. 56, no. 3, pp. 12–18, Mar. 2018.

[5] T. Kimura, M. Omura, Y. Kishimoto, and K. Hashimoto, "Comparative study of acoustic wave devices using thin piezoelectric plates in the 3–5-GHz range," *IEEE Trans. Microw. Theory Techn.*, vol. 67, no. 3, pp. 915–921, Jan. 2019.

[6] K. Hashimoto, *Surface Acoustic Wave Devices in Telecommunications: Modelling and Simulation*. Berlin, Germany: Springer-Verlag, 2013.

[7] R. Ruby, "A snapshot in time: The future in filters for cell phones," *IEEE Microw. Mag.*, vol. 16, no. 7, pp. 46–59, Aug. 2015.

[8] K. Hashimoto, *RF Bulk Acoustic Wave Filters for Communications*. Norwood, MA, USA: Artech House, 2009.

[9] G. Piazza, P. J. Stephanou, and A. P. Pisano, "Single-chip multiple-frequency ALN MEMS filters based on contour-mode piezoelectric resonators," *J. Microelectromech. Syst.*, vol. 16, no. 2, pp. 319–328, Apr. 2007.

[10] S. Menendez, P. de Paco, R. Villarino, and J. Parron, "Closed-form expressions for the design of ladder-type FBAR filters," *IEEE Microw. Wireless Compon. Lett.*, vol. 16, no. 12, pp. 657–659, Dec. 2006.

[11] M. Kadota and S. Tanaka, "Wideband acoustic wave resonators composed of hetero acoustic layer structure," *Jpn. J. Appl. Phys.*, vol. 57, no. 7S1, Jul. 2018, Art. no. 07LD12.

[12] M. Kadota, Y. I. Yunoki, T. Shimatsu, M. Uomoto, and S. Tanaka, "Suprious-free, near-zero-TCF hetero acoustic layer (HAL)SAW resonators using $LiTaO_3$ thin plate on quartz," in *Proc. IEEE Int. Ultrason. Symp.*, Oct. 2018, pp. 1–9.

[13] T. Takai *et al.*, "IHP SAW technology and its application to microacoustic components," in *Proc. IEEE Int. Ultrason. Symp*, Sep. 2017, pp. 1–8.

[14] T. Kimura *et al.*, "A high velocity and wideband SAW on a thin $LiNbO_3$ plate bonded on a Si substrate in the SHF range," in *Proc. IEEE Int. Ultrason. Symp. (IUS)*, Oct. 2019, pp. 1239–1248.

[15] M. Akiyama, T. Kamohara, K. Kano, A. Teshigahara, Y. Takeuchi, and N. Kawahara, "Enhancement of piezoelectric response in scandium aluminum nitride alloy thin films prepared by dual reactive cosputtering," *Adv. Mater.*, vol. 21, no. 5, pp. 593–596, Feb. 2009.

[16] M. Bousquet *et al.*, "Single-mode high frequency $LiNbO_3$ film bulk acoustic resonator," in *Proc. IEEE Int. Ultrason. Symp. (IUS)*, Oct. 2019, pp. 84–87.

[17] T. Yokoyama, Y. Iwazaki, Y. Onda, T. Nishihara, Y. Sasajima, and M. Ueda, "Highly piezoelectric co-doped AlN thin films for wideband FBAR applications," *IEEE Trans. Ultrason., Ferroelectr., Freq. Control*, vol. 62, no. 6, pp. 1007–1015, Jun. 2015.

[18] Y. Shen, P. Patel, R. Vetury, and J. B. Shealy, "452 MHz bandwidth, high rejection 5.6 GHz UNII XBAW coexistence filters using doped AlN-on-Silicon," in *IEDM Tech. Dig.*, Dec. 2019.

[19] L. Colombo, A. Kochhar, C. Xu, G. Piazza, S. Mishin, and Y. Oshmyansky, "Investigation of 20% scandium-doped aluminum nitride films for MEMS laterally vibrating resonators," in *Proc. IEEE Int. Ultrason. Symp. (IUS)*, Sep. 2017, pp. 1–4.

[20] M. Park, Z. Hao, D. G. Kim, A. Clark, R. Dargis, and A. Ansari, "A 10 GHz single-crystalline scandium-doped aluminum nitride Lamb-wave resonator," in *Proc. Transducers*, 2019, pp. 450–453.

[21] C. Zuo, C. He, W. Cheng, and Z. Wang, "Hybrid filter design for 5G using IPD and acoustic technologies," in *Proc. IEEE Int. Ultrason. Symp. (IUS)*, Oct. 2019, pp. 269–272.

[22] D. Psychogiou, R. Gómez-García, R. Loeches-Sánchez, and D. Peroulis, "Hybrid acoustic-wave-lumped-element resonators (AWLRs) for high-*Q* bandpass filters with quasi-elliptic frequency response," *IEEE Trans. Microw. Theory Techn.*, vol. 63, no. 7, pp. 2233–2244, 2015.
[23] X. Lu, K. Mouthaan, and Y. T. Soon, "Wideband bandpass filters with SAW-Filter-Like selectivity using chip SAW resonators," *IEEE Trans. Microw. Theory Techn.*, vol. 62, no. 1, pp. 28–36, Jan. 2014.
[24] M. Kadota, T. Ogami, K. Yamamoto, H. Tochishita, and Y. Negoro, "High-frequency Lamb wave device composed of MEMS structure using $LiNbO_3$ thin film and air gap," *IEEE Trans. Ultrason., Ferroelectr., Freq. Control*, vol. 57, no. 11, pp. 2564–2571, Nov. 2010.
[25] Y. Yang, A. Gao, R. Lu, and S. Gong, "5 GHz lithium niobate MEMS resonators with high FoM of 153," in *Proc. IEEE 30th Int. Conf. Micro Electro Mech. Syst. (MEMS)*, Jan. 2017, pp. 942–945.
[26] V. Plessky, S. Yandrapalli, P. J. Turner, L. G. Villanueva, J. Koskela, and R. B. Hammond, "5 GHz laterally-excited bulk-wave resonators (XBARs) based on thin platelets of lithium niobate," *Electron. Lett.*, vol. 55, no. 2, pp. 98–100, Jan. 2019.
[27] R. Lu, Y. Yang, M.-H. Li, M. Breen, and S. Gong, "5-GHz anti-symmetric mode acoustic delay lines in lithium niobate thin film," *IEEE Trans. Microw. Theory Techn.*, vol. 68, no. 2, pp. 573–589, Feb. 2020.
[28] M. Kadota, T. Ogami, K. Yamamoto, Y. Negoro, and H. Tochishita, "High-frequency Lamb wave device composed of $LiNbO_3$ thin film," *Jpn. J. Appl. Phys.*, vol. 48, no. 7S, 2009, Art. no. 07GG08.
[29] R. S. Weis and T. K. Gaylord, "Lithium niobate: Summary of physical properties and crystal structure," *Appl. Phys. A, Solids Surf.*, vol. 37, no. 4, pp. 191–203, Aug. 1985.
[30] Y. Yang, R. Lu, L. Gao, and S. Gong, "4.5 GHz lithium niobate MEMS filters with 10% fractional bandwidth for 5G front-ends," *J. Microelectromech. Syst.*, vol. 28, no. 4, pp. 575–577, Aug. 2019.
[31] P. J. Turner *et al.*, "5 GHz band n79 wideband microacoustic filter using thin lithium niobate membrane," *Electron. Lett.*, vol. 55, no. 17, pp. 942–944, Aug. 2019.
[32] D. Morgan, *Surface Acoustic Wave Filters*. Amsterdam, The Netherlands: Elsevier, 2007.
[33] K. Shibayama, K. Yamanouchi, H. Sato, and T. Meguro, "Optimum cut for rotated Y-cut $LiNbO_3$ crystal used as the substrate of acoustic-surface-wave filters," *Proc. IEEE*, vol. 64, no. 5, pp. 595–597, May 1976.
[34] R. Lu, T. Manzaneque, Y. Yang, M.-H. Li, and S. Gong, "Gigahertz low-loss and wideband S0 mode lithium niobate acoustic delay lines," *IEEE Trans. Ultrason., Ferroelectr., Freq. Control*, vol. 66, no. 8, pp. 1373–1386, Aug. 2019.
[35] *IEEE Standard on Piezoelectricity*, Standard ANSI/IEEE Std 176-1987, 1988.
[36] B. A. Auld, *Acoustic Fields and Waves in Solids*. Melbourne, FL, USA: Krieger, 1990.
[37] R. Lu, M.-H. Li, Y. Yang, T. Manzaneque, and S. Gong, "Accurate extraction of large electromechanical coupling in piezoelectric MEMS resonators," *J. Microelectromech. Syst.*, vol. 28, no. 2, pp. 209–218, Apr. 2019.
[38] Y. Yang, R. Lu, and S. Gong, "A 1.65 GHz lithium niobate A1 resonator with electromechanical coupling of 14% and Q of 3112," in *Proc. IEEE Int. Conf. Micro Electro Mech. Syst.*, Jan. 2019, pp. 875–878.
[39] Y. Yang, R. Lu, T. Manzaneque, and S. Gong, "Toward ka band acoustics: Lithium niobate asymmetrical mode piezoelectric MEMS resonators," in *Proc. IEEE Int. Freq. Control Symp. (IFCS)*, May 2018, pp. 1–5.
[40] R. Lu, T. Manzaneque, Y. Yang, J. Zhou, H. Hassanieh, and S. Gong, "RF filters with periodic passbands for sparse Fourier transform-based spectrum sensing," *J. Microelectromech. Syst.*, vol. 27, no. 5, pp. 931–944, Oct. 2018.
[41] M. Akgul, A. Ozgurluk, and C. T. C. Nguyen, "RF channel-select micromechanical disk filters—Part II: Demonstration," *IEEE Trans. Ultrason., Ferroelectr., Freq. Control*, vol. 66, no. 1, pp. 218–235, Jan. 2019.
[42] D. A. Feld, R. Parker, R. Ruby, P. Bradley, and S. Dong, "After 60 years: A new formula for computing quality factor is warranted," in *Proc. IEEE Ultrason. Symp.*, Nov. 2008, pp. 431–436.
[43] R. Lu and S. Gong, "Study of thermal nonlinearity in lithium niobate-based MEMS resonators," in *Proc. 18th Int. Conf. Solid-State Sensors, Actuat. Microsyst. (TRANSDUCERS)*, Jun. 2015, pp. 8–11.

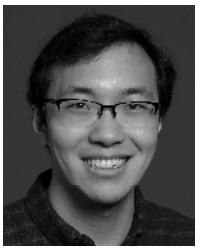

**Ruochen Lu** (Member, IEEE) received the B.E. degree (Hons.) in microelectronics from Tsinghua University, Beijing, China, in 2014, and the M.S. and Ph.D. degrees in electrical engineering from the University of Illinois at Urbana–Champaign, Urbana, IL, USA, in 2017 and 2019, respectively. He is currently a Post-Doctoral Researcher with the University of Illinois at Urbana–Champaign. His research interests include radio frequency microsystems and their applications for timing and signal processing. He received best student paper awards at the 2017 IEEE International Frequency Control Symposium and the 2018 IEEE International Ultrasonics Symposium. He was a recipient of the 2015 Lam Graduate Award from the College of Engineering at UIUC, the 2017 Nick Holonyak, Jr. Graduate Research Award, the 2018 Nick Holonyak, Jr. Fellowship, and the 2019 Raj Mittra Outstanding Research Award from the Department of Electrical and Computer Engineering at UIUC.

**Yansong Yang** (Member, IEEE) received the B.S. degree in electrical and electronic engineering from the Huazhong University of Science and Technology, Wuhan, China, in 2014, and the M.S. and Ph.D. degrees in electrical engineering from the University of Illinois at Urbana–Champaign, Urbana, IL, USA, in 2017 and 2019, respectively. He is currently a Post-Doctoral Researcher with from the University of Illinois at Urbana–Champaign. His research interests include design and microfabrication techniques of RF MEMS resonators, filters, switches, and photonic integrated circuits. He has won the Second Place in Best Paper Competition at the 2018 IEEE International Microwave Symposium and the Best Paper Award at 2019 IEEE International Ultrasonics Symposium. He was also a finalist for the Best Paper Award at the 2018 IEEE International Frequency Control Symposium. He was also a recipient of the 2019 P. D. Coleman Graduate Research Award from the Department of Electrical and Computer Engineering at UIUC.

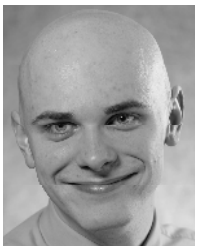

**Steffen Link** (Student Member, IEEE) received the B.S. degree in computer engineering from the South Dakota School of Mines and Technology, Rapid City, South Dakota, in 2018. He is currently pursuing the master's degree with the University of Illinois at Urbana–Champaign, Urbana, IL, USA. His research interests include design and microfabrication techniques of MEMS resonators, filters, and other radio frequency microsystems.

**Songbin Gong** (Senior Member, IEEE) received the Ph.D. degree in electrical engineering from the University of Virginia, Charlottesville, VA, USA, in 2010. He is currently an Associate Professor and the Intel Alumni Fellow with the Department of Electrical and Computer Engineering and the Micro and Nanotechnology Laboratory, University of Illinois at Urbana–Champaign, Urbana, IL, USA. His research primarily focuses on design and implementation of radio frequency microsystems, components, and subsystems for reconfigurable RF front ends. In addition, his research explores hybrid microsystems based on the integration of MEMS devices with photonics or circuits for signal processing and sensing. He was a recipient of the 2014 Defense Advanced Research Projects Agency Young Faculty Award, the 2017 NASA Early Career Faculty Award, the 2019 UIUC College of Engineer Dean's Award for Excellence in Research, and the 2019 Ultrasonics Early Career Investigator Award. Along with his students and post-doctoral researchers, he received the best paper awards from the 2017 and 2019 IEEE International Frequency Control Symposium, the 2018 and 2019 International Ultrasonics Symposium, and won the Second place in Best Paper Competition at the 2018 IEEE International Microwave Symposium. He is currently a Technical Committee Member of MTT-21 RF-MEMS of the IEEE Microwave Theory and Techniques Society, the International Frequency Control Symposium, and International Electron Devices Meeting. He also serves as the Chair of MTT TC2 and TC 21 and an Associate Editor for T-UFFC and JMEMS.